universe

MDPI

Article

A Simulation Study of Gravitational Redshift Tests and Geopotential Determination Using GNSS Undifferenced Carrier Phase Observations for the China Space Station

Wei Xu [1,2,*], Pengfei Zhang [2], Xiaoming Li [1] and Jia Song [1]

[1] School of Geographic Engineering and Spatial Information, Chuzhou University, Chuzhou 239000, China
[2] School of Geodesy and Geomatics, Wuhan University, Wuhan 430079, China
* Correspondence: whuxwei@whu.edu.cn

Abstract

The gravitational redshift test is a key means of testing general relativity and linking time-frequency signals with the geopotential, while geopotential determination is a core component of fundamental research in geodesy. The two are closely related in physical mechanism and mutually reinforcing. In this simulation study, based on the high-precision optical clock experimental platform onboard the Mengtian experimental module of the China Space Station (CSS), the models and methods for gravitational redshift testing and geopotential determination using CSS GNSS undifferenced carrier phase time-frequency signals are studied. Observation data from four ground stations and the CSS over one continuous week are selected, and GNSS observations and precise optical clock offsets are simulated to construct a GNSS time-frequency comparison experiment between space and ground. The simulation results show that the gravitational redshift test based on GNSS undifferenced carrier phase time-frequency comparison can reach 6.1×10^{-7}, with a standard deviation of 3.1×10^{-7}. With the EGM2008 gravity field model values as a reference, the root mean square deviation between the geopotential retrieved from GNSS undifferenced carrier phase time-frequency comparison and the model values is 2.5 m^2/s^2, further verifying the feasibility of geopotential determination using CSS-ground GNSS time-frequency signals. With the continuous improvement of clock performance, centimeter-level geopotential determination of equivalent height using high-precision space-borne optical clocks will gradually become possible in the future, and is expected to promote the unification of the global height datum.

Keywords: gravitational redshift; geopotential; CSS; GNSS; undifferenced; carrier phase; time-frequency signals

Check for updates

Academic Editors: Jiacheng Liu and Shilong Liao

Received: 16 October 2026
Revised: 9 November 2026
Accepted: 16 November 2026
Published: 17 November 2026

Copyright: © 2026 by the authors. Licensee MDPI, Basel, Switzerland. This article is an open access article distributed under the terms and conditions of the Creative Commons Attribution (CC BY) license.

1. Introduction

According to general relativity, clocks at different gravitational potentials tick at different rates, and frequency signals exchanged between two locations undergo a gravitational redshift. Based on this effect, relativistic time-frequency geodesy has been proposed, in which high-precision atomic or optical clocks are compared to infer the geopotential difference or height difference between two sites. With the frequency stability and systematic uncertainty of optical clocks reaching the 10^{-18} level [1,2], this makes the use of high-precision time-frequency signals for gravitational redshift tests and geopotential determination a current research hotspot. Among various time-frequency comparison techniques, GNSS carrier phase observations offer global coverage, continuous availability,

and low cost, and thus provide a promising opportunity for precise geopotential determination. The China Space Station (CSS), Mengtian experimental module equipped with an SI optical clock, offers a new space-based platform for GNSS observations and enables continuous ground-to-space time-frequency comparison. However, gravitational redshift tests and geopotential determination based on GNSS observations of CSS remain largely unexplored.

In terms of gravitational redshift tests, numerous experiments have been carried out over the past decades. The phenomenological parameter α is adopted in gravitational redshift tests to quantify departures from local position invariance (LPI). Gravitational redshift experiments aim to constrain $|\alpha|$. The Pound–Rebka–Snider [3,4] experiment in the 1960s first verified the gravitational redshift using the Mössbauer effect over a height difference of 23 m, with an accuracy of about 10^{-2}. The 1971 atomic clock experiment on commercial aircraft confirmed that the clock difference agreed with relativistic predictions. The Gravity Probe A (GP-A) experiment [5–7] sent a hydrogen maser to an altitude of about 10,000 km and obtained a test accuracy of about 1.4×10^{-4}. With the development of precision optical and atomic clocks, ground-based tests have advanced. Chou et al. [8] performed a gravitational redshift test by elevating a clock by 30 cm and observing for 40 h, with a relative accuracy of about 34%; Grotti et al. [9] carried out a remote comparison of movable optical clocks with an accuracy of 1.7%; and Takamoto et al. [10] conducted a gravitational redshift test using a movable optical clock at the Tokyo Skytree in 2020, achieving a result of $(1.49 \pm 9.1) \times 10^{-5}$. More recently, Li et al. [11] reported a gravitational redshift measurement experiment using a satellite-borne compact passive hydrogen maser (PHM) in a lunar distant retrograde orbit (DRO), and the measured gravitational redshift parameter is $(8.74 \pm 4.17) \times 10^{-3}$. In addition, based on clock offsets from GPS and Galileo satellites, relevant scholars have conducted a large number of gravitational redshift testing experiments [12–16]. One of the most precise results to date was obtained in 2018 from the analysis of satellite clock data of the Galileo E202 (E14) and E201 (E18) hydrogen masers, giving $(0.91 \pm 2.48) \times 10^{-5}$ [17].

Geopotential determination based on time-frequency signals has developed in parallel with gravitational redshift tests. Early studies mainly used optical fibers or coaxial cables to connect high-precision clocks. For example, Chou et al. [8] connected two optical clocks with a fiber link over a height difference of 33 cm and inferred a height difference deviation of 4 cm with an accuracy of 15 cm; Takano et al. [18] connected three optical clocks with a 30 km fiber link and obtained a height difference uncertainty of about 6.0 cm; Lisdat et al. [19] compared Sr optical clocks between the Paris Observatory and PTB over a 1415 km fiber link with a frequency stability of 5×10^{-17} and obtained a height difference uncertainty of 4 cm; Grotti et al. [9] used a movable optical clock with a frequency stability of 7×10^{-17} for fiber-based height difference determination, with a deviation of tens of centimeters from leveling; Shen et al. [20] simulated fiber frequency transfer with a 10^{-19} optical clock and showed a theoretical accuracy of 1.5 cm; Takamoto et al. [10] carried out a clock transport experiment at the Tokyo Skytree with a height difference of about 450 m and obtained a height difference uncertainty of about 4 cm. Huang et al. [21], Liu et al. [22], and Yuan et al. [23] have used a movable optical clock to achieve decimeter-level height difference measurement accuracy. Lee et al. [24] used GNSS, leveling, gravity, GGM, and local geoid models with a KRISS-Yb1 atomic clock for altitude determination, with an uncertainty of 4 cm. Limited by the cost and terrain constraints of fiber and coaxial cables, GNSS time-frequency comparison has brought new opportunities for precise geopotential determination. Xu et al. [25], Wang et al. [26], and Wu et al. [27] used GNSS carrier phase observations and a single hydrogen maser or a pair of hydrogen masers between Wuhan and Xianning, China, and achieved a geopotential accuracy of about 5.0 m^2/s^2 using GNSS undifferenced time-frequency

comparison. Xu et al. [28] and Wu et al. [29] further simulated optical clock differences and showed that the equivalent height accuracy of GNSS time-frequency comparison can reach the decimeter level.

With the development of space-borne clocks, simulation gravitational redshift tests and geopotential determination studies based on the Atomic Clock Ensemble in Space (ACES) and CSS have also been carried out. Savalle et al. [30] showed that a target gravitational redshift test uncertainty of 3×10^{-6} can be reached after several measurement sessions of 20 days. Sun et al. [31] proposed a tri-frequency combination method based on ACES microwave links and achieved 2×10^{-6}. Shen et al. [32] carried out a gravitational redshift test based on the CSS optical clock and reached 5×10^{-7}. Zhang et al. [33] evaluated the effects of second- and third-order ionospheric delays on ACES and CSS gravitational redshift tests and concluded that the third-order term is negligible. Qin et al. [34] proposed equipping a deep-space hydrogen maser in China's Lunar Exploration Project and reached an uncertainty of 3.7×10^{-7} after a 60 d session. Xu et al. [35] achieved a gravitational redshift test precision of $(1.8 \pm 47) \times 10^{-7}$ using laser time links. Dai et al. [36] simulated a gravitational redshift test by comparing phase signals between CSS and the ground station and obtained a constraint on the GRS violation parameter of $(0.14 \pm 4.65) \times 10^{-7}$. Enzer and Yu [37] reported a frequency approach to analyze ACES space-clock-to-ground comparison data and constrained the gravitational-redshift violation parameter to better than 2.9×10^{-6} from 12 d of simulated data. Zhang et al. [38] studied a dual-frequency signal frequency transfer model for geopotential determination based on the CSS optical clock and achieved 0.6 ± 1.2 m^2/s^2 at a cutoff elevation of 15°. Zhang et al. [39] then proposed an improved tri-frequency microwave frequency combination method and achieved 0.7 m^2/s^2 with EGM2008 as the truth. Klarissa et al. [40] simulated geopotential determination of ground stations based on ACES microwave links and showed that optical links enable faster convergence, reaching decimeter-level height accuracy within a few days and centimeter-level accuracy over longer periods.

Although extensive studies have been carried out based on CSS, most of them rely on ground stations receiving microwave or laser signals transmitted from CSS. Due to CSS moving fast and having a short orbital period, ground stations cannot continuously observe CSS signals, and the gravitational redshift test and geopotential determination often require data concatenation and longer observation time. Since CSS is equipped with high-precision GNSS time-frequency receivers, using GNSS time as a bridge will help solve the problem of interrupted ground observations and enable continuous observation. However, gravitational redshift tests and geopotential determination based on GNSS time-frequency comparison between CSS and ground stations remain blank, and their accuracy still needs to be evaluated.

To address these issues, this research focuses on gravitational redshift testing and geopotential determination based on GNSS observations of the CSS. First, the GNSS undifferenced carrier phase time-frequency comparison model between CSS and ground stations is established. Then, the gravitational redshift test and geopotential determination are carried out using the proposed model. Finally, the accuracy and feasibility of the method are evaluated through simulations and analyses.

2. Methods

2.1. GNSS Undifferenced Time-Frequency Comparison

The undifferenced pseudo-range and carrier phase observations of GPS and BDS can be expressed as [41]:

$$\begin{cases} P_{r,j}^{S,i} = \rho_r^{S,i} + c\left(dt_r^S - dt^{S,i}\right) + MW_r^{S,i} \cdot ZWD_r \\ \quad +\gamma_j^{S,i} \cdot I_{r,1}^{S,i} + d_{r,j}^{S,i} - d_j^{S,,i} + \zeta_{r,j}^{S,i} \\ L_{r,j}^{S,i} = \rho_r^{S,i} + c\left(dt_r^S - dt^{S,i}\right) + MW_r^{S,i} \cdot ZWD_r \\ \quad -\gamma_j^{S,i} \cdot I_{r,1}^{S,i} + \lambda_j^{S,i} \cdot \left(N_{r,j}^{S,i} + b_{r,j}^S - b_j^{S,i}\right) + \xi_{r,j}^{S,i} \end{cases} \tag{1}$$

where P and L refer to code and phase measurements in units of meters, respectively. The superscripts i and S correspond to the i-th satellite belonging to system S (e.g., GPS and BDS). The subscripts r and j stand for the receiver and frequency indices, respectively; λ is the wavelength associated with frequency j; ρ is the geometric range separating the satellite and receiver; dt_r and dt^s represent receiver and satellite clock offsets in seconds, respectively; MW refers to the wet mapping function; ZWD is the tropospheric zenith wet delay; I stands for slant ionospheric delay; γ denotes frequency-dependent scaling factors for ionospheric delay; N is the integer carrier phase ambiguity; d is the receiver un-calibrated code delay (UCD) in meters; b denotes un-calibrated phase delay (UPD) in cycles; ζ and ξ correspond to pseudo-range and carrier phase observation noise terms, respectively.

With precise satellite orbits, satellite clock offsets, and satellite differential code bias products adopted, the first-order ionospheric delay is removed using the dual-frequency ionosphere-free (IF) combination. Considering the time system bias between GPS and BDS, GPS Time (GPST) is taken as the datum, and the inter-system bias (ISB) parameter is introduced. The linearized GPS/BDS combined undifferenced carrier phase time-frequency comparison model can be expressed as follows:

$$\begin{cases} p_{r,IF}^{GPS,i} = \boldsymbol{\mu}_r^{GPS,i} \cdot \mathbf{x} + c\tilde{dt}_r^{GPS} + MW_r^{GPS,i} \cdot ZWD_r + \zeta_{r,IF}^{GPS,i} \\ l_{r,IF}^{GPS,i} = \mathbf{u}_r^{GPS,i} \cdot \mathbf{x} + c\tilde{dt}_r^{GPS} + MW_r^{GPS,i} \cdot ZWD_r + \lambda_{IF}^{GPS,i} \cdot \widetilde{N}_{r,IF}^{GPS,i} + \xi_{r,IF}^{GPS,i} \\ p_{r,IF}^{BDS,i} = \boldsymbol{\mu}_r^{BDS,i} \cdot \mathbf{x} + c\tilde{dt}_r^{GPS} + MW_r^{BDS,i} \cdot ZWD_r + ISB + \zeta_{r,IF}^{BDS,i} \\ l_{r,IF}^{BDS,i} = \mathbf{u}_r^{BDS,i} \cdot \mathbf{x} + c\tilde{dt}_r^{GPS} + MW_r^{BDS,i} \cdot ZWD_r + \lambda_{IF}^{BDS,i} \cdot \widetilde{N}_{r,IF}^{BDS,i} + \xi_{r,IF}^{BDS,i} \end{cases} \tag{2}$$

with

$$\begin{cases} c\tilde{dt}_r^{GPS} = cdt_r + d_{r,IF}^{GPS} \\ ISB = d_{r,IF}^{BDS} - d_{r,IF}^{GPS} \\ \lambda_{IF}^{GPS/BDS} \cdot \widetilde{N}_{r,IF}^{GPS/BDS,i} = \lambda_{IF}^{GPS/BDS} \cdot \left(N_{r,IF}^{GPS/BDS,i} + b_{r,IF}^{GPS/BDS} - b_{IF}^{GPS/BDS,i}\right) - d_{r,IF}^{GPS/BDS} \end{cases} \tag{3}$$

where p and l denote the observed-minus-computed quantities for pseudo-range and carrier phase measurements, respectively; $\mathbf{u}$ stands for the line-of-sight direction cosine; $\mathbf{x}$ refers to the coordinate correction vector with respect to the receiver's approximate coordinates. The tilde symbol "~" denotes re-parameterized unknowns, while the subscript "IF" indicates the ionosphere-free combination. Hence, the parameters to be estimated include $[\mathbf{x}, c\tilde{dt}_r^{GPS}, ZWD_r, ISB, \widetilde{N}_{r,IF}^{GPS,i}, \widetilde{N}_{r,IF}^{BDS,i}]$.

To fix the undifferenced ambiguity, satellite-side UPD corrections can be applied to the raw observations using the phase bias products provided by Wuhan University, thereby yielding IF ambiguities free of satellite UPD effects. These are then formed into inter-satellite single-differenced (SD) IF ambiguities, from which the inter-satellite SD wide-lane and narrow-lane ambiguities are resolved, thereby restoring the integer property of the inter-satellite SD IF ambiguities. With these serving as constraints to update the parameters, the receiver clock offset is ultimately obtained under the ambiguity-fixed solution [42].

When performing GNSS time-frequency comparison between the ground station Q and CSS, the time difference $\Delta t_{CSS,Q}$ between the Q and CSS can be expressed as:

$$\Delta t_{CSS,Q} = \tilde{dt}^{GPS}_{Q} - \tilde{dt}^{GPS}_{CSS} = dt_Q - dt_{CSS} + \left(d^{GPS}_{Q,IF} - d^{GPS}_{CSS,IF}\right)/c \quad (4)$$

where dt_Q and dt_{CSS} denote the local clock times of ground station Q and the CSS, respectively; $\tilde{dt}_Q$ and $\tilde{dt}_{CSS}$ denote the station Q and CSS receiver clock offsets derived from the GNSS undifferenced time-frequency comparison model, respectively. In practice, GNSS time-frequency comparison realizes local time comparison by taking the time scale of the International GNSS Service (IGS) satellite clock offset products (IGST) as the bridge. The time comparison results between the two sites are affected by receiver UCD. Relevant studies have demonstrated that receiver UCDs are relatively stable and can be treated as constants, which only induce a constant deviation in the local time comparison results. For GNSS precise timing applications, receiver UCDs can be calibrated in advance to eliminate their adverse effects on time comparison accuracy.

2.2. Geopotential Determination and Gravitational Redshift Testing Using Time-Frequency Signals

2.2.1. Geopotential Determination via Time-Frequency Signals

In accordance with the framework of general relativity, the ticking frequency of a clock is strongly correlated with the geopotential at its location. Assume that clocks Clk_Q, CLK_{CSS}, and Clk_{Geoid} are placed at the ground station Q, CSS, and the geoid, respectively. After Clk_{Geoid} measures a time interval dt_{Geoid}, the time readings dt_Q and dt_{CSS} recorded by CLK_Q and CLK_{CSS} can be formulated as [43]:

$$dt_{CSS/Q} = \left(1 + \frac{\Delta W_{Geoid,CSS/Q}}{c^2}\right) dt_{Geoid} \quad (5)$$

with

$$\Delta W_{Geoid,CSS/Q} = W_{CSS/Q} - W_{Geoid} \quad (6)$$

where ΔW denotes the geopotential difference between the two stations, W_Q, W_{CSS} and W_{Geoid} represent the geopotentials of CLK_Q, CLK_{CSS} and Clk_{Geoid}, respectively.

After a standard time duration T, the time difference $\Delta t_{CSS,Q}$ between the ground station Q and CSS can be expressed as:

$$\Delta t_{CSS,Q} = \int_0^T \left(1 + \frac{\Delta W_{Geoid,CSS}}{c^2}\right) dt_0 - \int_0^T \left(1 + \frac{\Delta W_{Geoid,Q}}{c^2}\right) dt_{Geoid} = -T\frac{\Delta W_{CSS,Q}}{c^2} \quad (7)$$

Equation (7) is equivalent to:

$$\Delta f_{CSS,Q} = f_Q - f_{CSS} = -\frac{\Delta W_{CSS,Q}}{c^2} f \quad (8)$$

where $\Delta f_{CSS,Q}$ is the gravity frequency shift between two clocks at Q and CSS, f_Q and f_{CSS} are the oscillation frequencies of CLK_Q and CLK_{CSS}, respectively, and f represents the reference frequency.

The geopotential difference between Q and CSS can be expressed as:

$$\Delta W_{CSS,Q} = W_{CSS} - W_Q = -\frac{\Delta t_{CSS,Q}}{T} c^2 = -\frac{\Delta f_{CSS,Q}}{f} c^2 \quad (9)$$

Based on Equation (9), the geopotential at ground station Q can be determined provided that the geopotential of the CSS is known.

2.2.2. Gravitational Redshift Testing via Time-Frequency Signals

The essence of testing the gravitational redshift using time-frequency signals is to measure the relative frequency shift $\Delta f'_{CSS,Q}/f$ between two clocks at Q and CSS caused by the difference in gravitational potential. The deviation in the relative frequency shift of clocks induced by gravitational potential variation can be modeled as [35]:

$$\frac{\Delta f'_{CSS,Q}}{f} = (1+\alpha)\frac{\Delta V_{CSS,Q}}{c^2} \tag{10}$$

with

$$\Delta V_{CSS,Q} = \Delta W_{CSS,Q} - \Delta\Phi_{CSS,Q} \tag{11}$$

where α is a dimensionless coefficient that quantifies any violation of Einstein's equivalence principle of LPI. If LPI holds, then $\alpha = 0$. $\Delta V_{CSS,Q}$ and $\Delta\Phi_{CSS,Q}$ are the gravitational potential difference and centrifugal potential difference between station Q and the *CSS*, respectively. Moreover, $\Delta W_{CSS,Q}$ can be determined via Equation (9), and $\Delta\Phi_{CSS,Q}$ can be calculated from the rotation angular velocity and the perpendicular distance to the rotation axis.

Let $\Delta\overline{V}_{CSS,Q}$ be the theoretical value of gravitational potential difference between the ground station Q and CSS. Equation (10) can then be further rewritten as:

$$\alpha = \frac{\Delta V_{CSS,Q} - \Delta\overline{V}_{CSS,Q}}{\Delta\overline{V}_{CSS,Q}} \tag{12}$$

2.3. Implementation Process of GNSS Undifferenced Time-Frequency Comparison for Gravitational Redshift Test and Geopotential Determination

Figure 1 illustrates the workflow of GNSS undifferenced time-frequency comparison for gravitational redshift test and geopotential determination. Receivers at the ground station and the CSS are externally connected to high-precision optical clocks simultaneously. The optical clocks provide 1 PPS and 10 Hz signals as the external frequency references for the receivers to carry out GNSS observations. Using the acquired GNSS observations from the ground station and CSS, the receiver clock offsets of the ground station and CSS are accurately estimated with the GNSS undifferenced time-frequency comparison model presented in Section 2.1, together with IGS products including satellite clock offsets, orbits, and DCBs, as well as error correction models (e.g., tidal models and the Sagnac model). Taking IGS product time as the time bridge, the two estimated clock offsets are differenced to obtain the time difference $\Delta t_{CSS,Q}$ between the CSS and the ground station. The geopotential difference between the spaceborne and ground sites is then derived according to the relationship between potential difference and time difference in Equation (9). If the geopotential of CSS W_{CSS} is known, the geopotential W_Q of the ground can be determined. The centrifugal potential difference between the two sites is removed using Equation (11) to yield the gravitational potential difference $\Delta V_{CSS,Q}$. Finally, the gravitational potential difference obtained from GNSS time comparison is differenced from its theoretical value, and the coefficient for the gravitational redshift test between the ground and space is calculated via Equation (12).

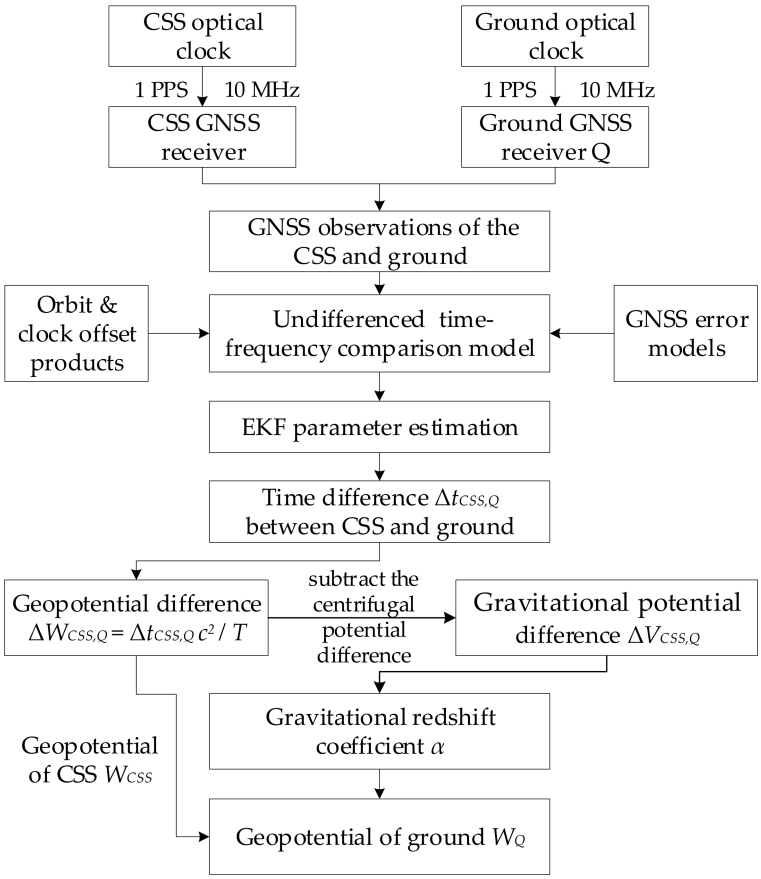


Figure 1. Flow chart of GNSS undifferenced time-frequency comparison for gravitational redshift test and gravitational potential determination.

3. Simulation of Optical Clock Offset and GNSS Observations

3.1. Simulation of Optical Clock Offset

Although the Mengtian experimental module of the CSS has been in orbit since 2022, the optical clock is still in testing with no complete measured observational data available. Therefore, this research constructs simulated observation sequences for gravitational redshift tests and geopotential determination experiments based on CSS-ground station GNSS time-frequency comparison.

Atomic clock noise is generally formed by the linear superposition of five types of noise. Relevant studies [39] show that the noise of optical clocks is dominated by WFM and FFM, among which WFM noise is the primary component, and the frequency drift of atomic clocks can be neglected. A two-dimensional stochastic differential equation is adopted to characterize the evolution of clock offset corresponding to WFM, while FFM flicker frequency modulation noise is superimposed onto the clock signal as an independent component. The expression of the two-dimensional stochastic differential equation is [44]:

$$\begin{cases} dX_1(t) = (X_2(t) + \mu_1)dt + \sigma_1 dW_1(t) \\ dX_2(t) = \mu_2 dt \\ X_1(0) = c_1 \\ X_2(0) = c_2 \end{cases} \quad t \geq 0 \tag{13}$$

Here, X_1 denotes the clock offset, while X_2 corresponds to the frequency offset. The parameters μ_1 and μ_2 serve as drift parameters associated with the Wiener stochastic processes. Specifically, μ_1 characterizes the static initial frequency bias, commonly denoted

by y_0; μ_2 stands for the frequency drift coefficient a. From metrological conventions, the relations $c_2 + \mu_1 = y_0$ and $\mu_2 = a$ hold. The diffusion coefficient σ_1 governs the magnitude of WFM noise. $W_1(t)$ refers to the Wiener process for X_1, corresponding to WFM.

The Allan deviation (ADEV) of the clock is synthesized by the combined contributions of WFM and FFM noise, which can be formulated as [45]:

$$\begin{cases} \sigma_y^{WFM}(\tau) = \sigma_1/\sqrt{\tau} \\ \sigma_y^{FFM}(\tau) = \sigma_2 \end{cases} \tag{14}$$

where σ^{WFM} and σ^{FFM} represent the Allan deviations associated with WFM and FFM at averaging time τ, respectively, and σ_2 is the constant Allan deviation floor of FFM noise independent of averaging time τ.

According to the design specifications of the CSS SI optical clock [32], in this study, the σ_1 and σ_2 corresponding to WFM and FFM for the CSS optical clock are set to 2.0×10^{-15} and 2.0×10^{-18}, respectively. For ground station optical clocks, σ_1 and σ_2 are set to 1.0×10^{-15} and 2.0×10^{-18}. The Stable32 software (http://www.stable32.com/) is used to simulate the clock offsets of the CSS and ground station optical clocks.

As shown in Figure 2, the second-level frequency stabilities of the CSS and ground station optical clocks are 1×10^{-15} and 2×10^{-15}, respectively, which are consistent with their white frequency modulation (WFM) parameters. For the simulated CSS optical clock (adopting the official design specifications), the frequency stability reaches 3.0×10^{-17} at an averaging time of 4000 s [32,46]. When the averaging time increases to 100,000 s and 200,000 s, the frequency stability of the simulated CSS optical clock is 7.6×10^{-18} and 5.4×10^{-18}, respectively. Its day-averaged stability is 8.0×10^{-18}, which meets the design specification of the physical CSS optical clock (with a day-averaged stability of approximately 8.0×10^{-18}). For the ground optical clock, the frequency stability reaches 2.7×10^{-18} at averaging times of 100,000 s and 200,000 s, satisfying the design target for laboratory optical clocks. Notably, the frequency stability curves of the CSS and GS optical clocks show a slight upturn for averaging times longer than 10,000 s, which is attributed to FFM noise.

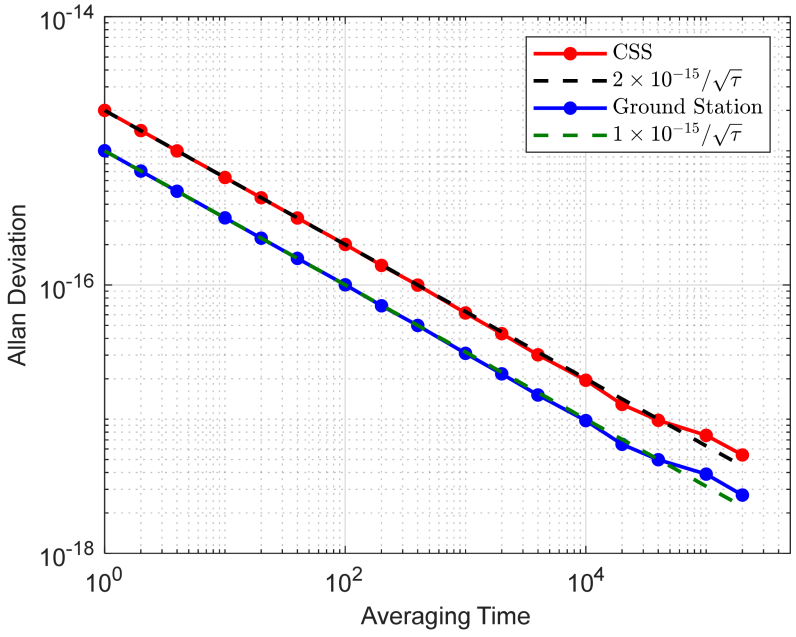


Figure 2. Frequency stability of optical clocks at the space station and ground station.

3.2. Simulation of GNSS Observations

Figure 3 illustrates the workflow for GNSS observation simulation. The simulation and processing framework is built on a modified version of RTKLIB open-source software (https://www.rtklib.com, accessed on 15 November 2026). The coordinates of ground stations are extracted from the SNX files released by the IGS, the coordinates of CSS are obtained from the China Manned Space Engineering Office (https://www.cmse.gov.cn/gfgg/zgkjzgdcs/, accessed on 15 November 2026), and satellite positions are derived by interpolating Wuhan University (WHU) final precise orbit products. The geometric range between satellites and stations is calculated accordingly.

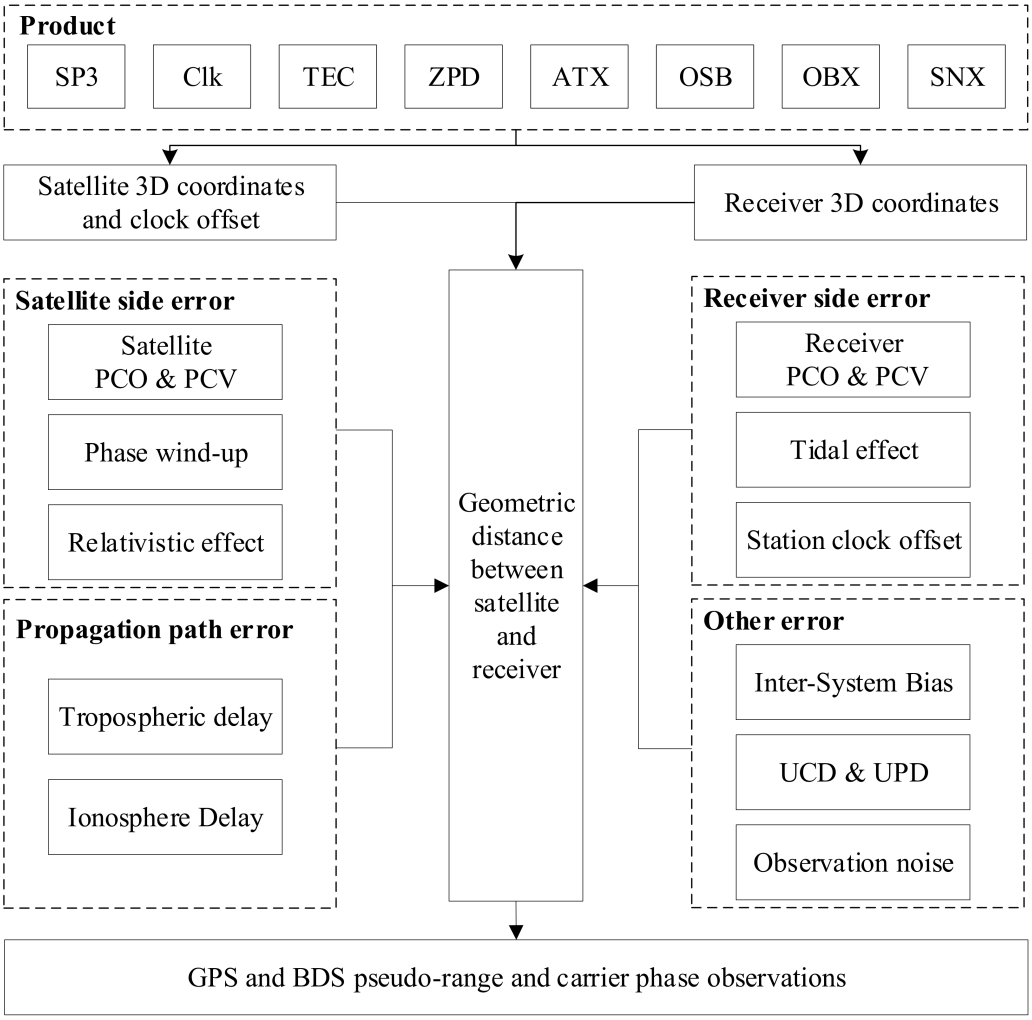


Figure 3. Simulation process of CSS and ground station GPS and BDS Observations.

The simulation of receiver-side errors is implemented as follows: station displacements caused by solid Earth tides, ocean loading tides, and polar tides are computed and superimposed using the IERS 2010 correction model [47,48]. CSS and ground station receiver antenna PCO and PCV correction parameters are obtained from the IGS igs20.atx antenna file. CSS and ground station receiver clock offsets are simulated based on a stochastic differential equation [44,45].

In terms of propagation path error simulation, the tropospheric dry delay at ground stations is calculated using the Saastamoinen model [49] combined with the GPT (Global Pressure and Temperature) model [50] and the GMF mapping function [51]. Tropospheric wet delay is acquired by interpolating IGS Zenith Path Delay (ZPD) products [52]. For CSS,

its orbital altitude is about 400 km, originally higher than the troposphere; tropospheric delay effects are neglected in the simulation. Ionospheric delay is obtained via interpolation of the GIM-TEC grid products released by IGS [53].

For satellite-side error simulation, satellite clock offsets are interpolated from WHU precise clock products. Satellite antenna PCO and PCV corrections are also taken from the igs20.atx antenna product. The ground station satellite antenna phase wind-up is calculated using the PhWu model, and the required satellite attitude data are read from ORBEX (ORBit EXchange, suffix OBX) files. Due to CSS's inability to obtain its satellite attitude, nominal attitude is used as a substitute in the simulation. Satellite-related relativistic effects, including relativistic effects for elliptical orbits, the Sagnac effect, and the Shapiro effect, are simulated using corresponding theoretical models. The UCD and UPD of satellites and receivers adopt the bias products from Wuhan University [54]. For multi-GNSS scenarios, stochastic constants are introduced to characterize ISBs of different navigation systems.

All errors from the receiver side, signal propagation path and satellite side are added to the satellite-station geometric range to generate pseudo range observations without random measurement noise. Noise-free carrier phase observations are further obtained by dividing the noise-free pseudo range by the carrier wavelength of the corresponding frequency. For each continuous observation arc, the initial value of carrier phase ambiguity is set as a random integer. The measurement noise of pseudo range and carrier phase is modeled as zero-mean Gaussian random noise, whose STD varies dynamically with satellite elevation angle. The STDs of pseudo range and carrier phase observations at the zenith are set to 0.3 m and 3.0 mm, respectively. The random noise is superimposed onto the noise-free observation sequence to finally realize the simulation of GNSS pseudo range and carrier phase observation data.

4. Experimental Setup and Data Processing Strategies

Four ground stations are selected for the gravitational redshift test and geopotential determination experiment, forming four time-frequency comparison links between the ground stations and CSS. The experiment spans DOY 180 to 186 of 2026, covering a total of 7 days, with an observation sampling interval of 30 s. Three of the selected stations are located in Europe and one in Africa. Among them, PTBB, OP71, and ONSA are stations of UTC time-keeping laboratories. Since this study uses GNSS time as a bridge to conduct time comparisons between CSS and ground stations for gravitational redshift verification and geopotential determination, it is not required that ground stations track CSS. The geographical distribution and basic information of the selected stations are shown in Figure 4 and Table 1. Although all selected IGS stations are equipped with high-precision cesium atomic clocks or hydrogen masers, their performance still fails to meet the accuracy requirements for gravitational redshift testing and geopotential determination. Therefore, while retaining the basic information of ground stations, this study simulates GNSS observations of the selected stations to replace the station clocks with high-precision optical clock data. The gravitational potential and geopotential information derived from the EGM2008 gravity field model [55] are adopted to evaluate the accuracy of gravitational redshift tests and geopotential determination using GNSS time-frequency signals. The strategy for GNSS undifferenced data processing is shown in Table 2.

Table 1. Basic information of experimental stations.

Station	Lat	Lon	Height	Receiver Type	Antenna Type
HARB	−25.89	27.71	1558.08	SEPT POLARX5TR	TRM59800.00
ONSA	57.40	11.93	45.50	SEPT POLARX5TR	AOAD/M_B

Table 1. *Cont.*

Station	Lat	Lon	Height	Receiver Type	Antenna Type
PTBB	52.30	10.46	130.20	SEPT POLARX5TR	LEIAR25.R4
WTZZ	49.14	12.88	665.90	JAVAD TRE_3 DELTA	LEIAR25.R3

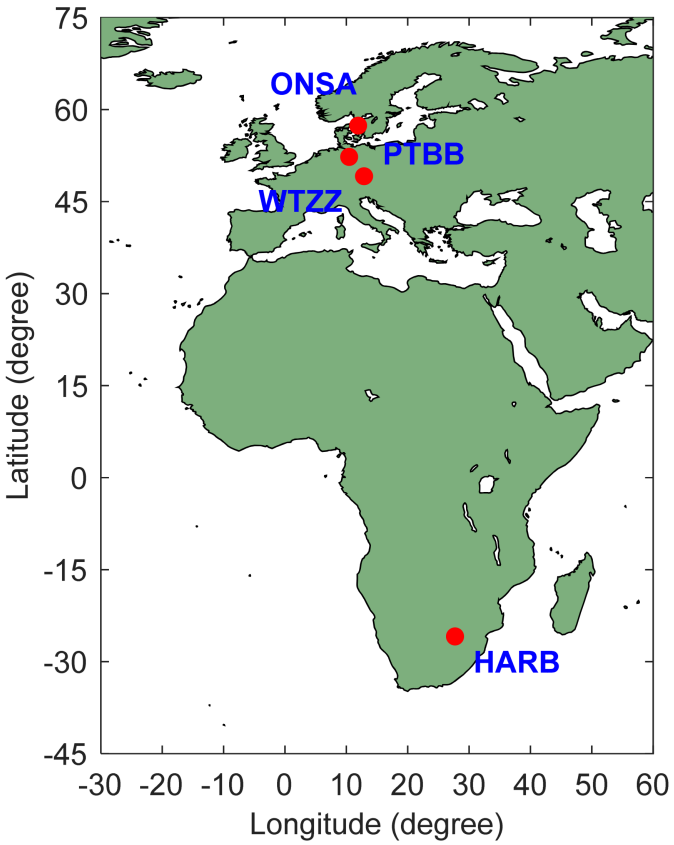


Figure 4. Geographical distribution of experimental stations.

Table 2. Data processing strategies for the experiment.

Item	Strategy
Observations	GPS: L1/L2; BDS-3: B1I/B3I
Filter	Forward-backward Kalman filter
Simple rate	30 s
Elevation cutoff	7°
orbit & clock	WHU precise products
Earth rotation	International Earth Rotation Service (IERS) convention [47]
Relativistic effect	Corrected: elliptical orbit and Shapiro effect [47]
Phase windup	Corrected by model [56]
Tide effect	Corrected [47,48]
Antenna error	Corrected, igs20.atx file
Inter-system bias	Estimated as constant
Station coordinate	Ground station, Static, estimated as constant; CSS, kinematic
Receiver clock	Estimated as white noise
Ionospheric delay	IF combination
Tropospheric delay	CSS: ignored; Ground station: dry delay correction using Saastamoinen model [49], wet delay as parameter estimation
Ambiguity	Estimated as a constant, fixed solution

5. Results

5.1. Number of Satellites and Dilution of Precision

Figure 5 shows the time series of visible satellites for the CSS and ground stations during the experiment. For each station, the number of visible satellites is approximately 9 for GPS and BDS individually. Under the combined GPS/BDS mode, the average number of visible satellites exceeds 18 for all stations, with a maximum of 27 and a minimum of 11 during the observation period. The ONSA station has the highest average number of combined visible satellites. As CSS operates in a high-speed dynamic environment, the time series of visible satellites presents larger fluctuations and more frequent variations compared with static ground stations. Restricted by ground stations' geographical location, BDS GEO and IGSO satellites have low elevation angles and poor visibility in this region. Meanwhile, the WHU precise products adopted in this study do not provide orbit and clock products for BDS GEO satellites, and only contain precise products for three BDS IGSO satellites. These combined factors lead to comparable visible satellite counts between BDS and GPS.

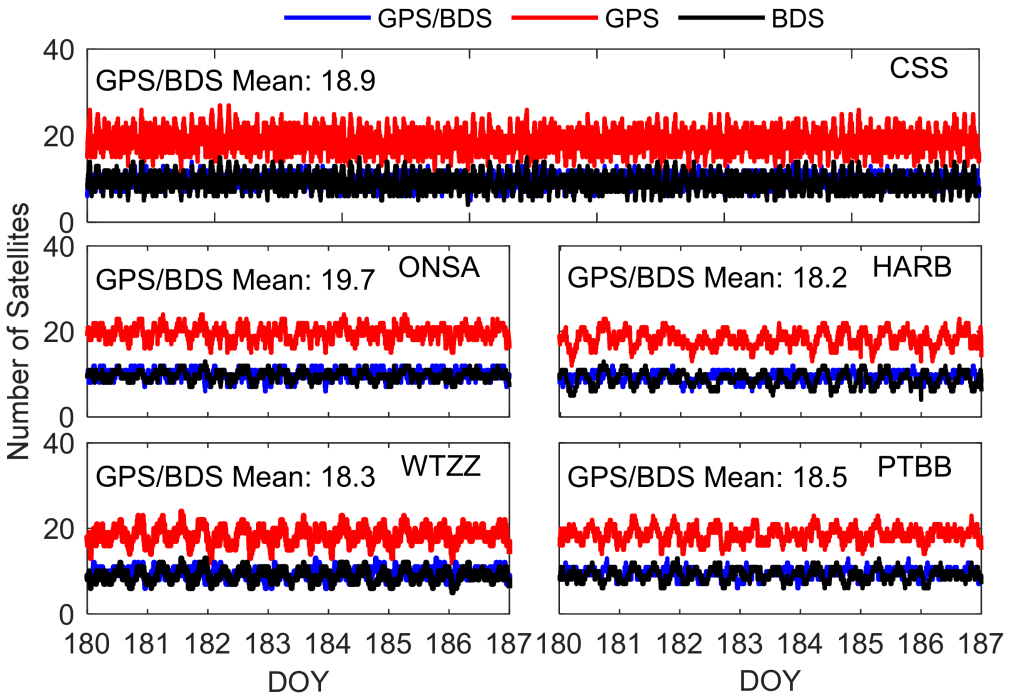


Figure 5. Time series of the number of satellites for CSS and ground stations.

Figure 6 illustrates the time series of PDOP and TDOP for the combined GPS/BDS system at each station during the experiment. It can be observed that the PDOP of all stations is maintained around 0.5, with the lowest mean PDOP at ONSA. The mean TDOP of each station is approximately 1.1. ONSA and PTBB share the same mean TDOP of 1.13, representing the optimal satellite geometry over time. The mean TDOP of CSS and WTZZ are 1.16 and 1.14, respectively. As CSS operates in a high-speed dynamic mode, its TDOP and PDOP time series fluctuate more frequently than those of static ground stations, which reflects the continuously varying satellite geometric configuration in the on-orbit scenario. Although the number of visible satellites changes rapidly for CSS, no obvious degradation is observed in its TDOP and PDOP. In addition, minor noise spikes appear in the DOP series at several epochs, but all values remain below 2.0. This behavior is related to the number of available satellites and their spatial distribution at corresponding epochs.

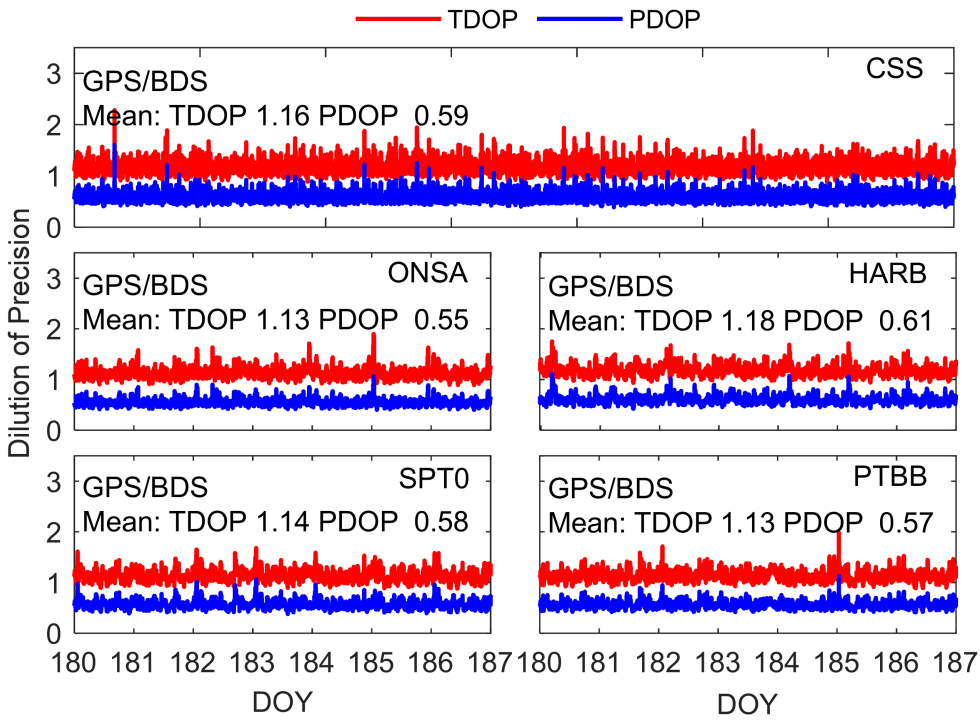


Figure 6. Time series of dilution of precision (DOP) of the combined GPS/BDS system for CSS and ground stations during the experiment.

5.2. Results of GNSS Undifferenced Time-Frequency Comparison

Figure 7 shows the clock offset, epoch-differenced clock offset results, and detrended residuals for the CSS-HARB link derived from GNSS undifferenced carrier phase time-frequency comparison. Due to the continuous dynamic variation of the geopotential at CSS, the clock offset series between CSS and the ground stations exhibits an obvious periodic trend, which is closely related to the periodic geopotential difference caused by the orbital period of CSS. Before DOY 183.3, the clock offset series generally shows a decreasing trend, while after DOY 183.3 it changes to an increasing trend. Correspondingly, the epoch-by-epoch differences of the clock offset also present a step-like change around DOY 183.3. After removing the trend component from the epoch-by-epoch differences, the resulting residuals approximately show white noise characteristics, which mainly originate from clock noise and GNSS observation noise. It can be seen that the comparison results of the float and fixed ambiguity solutions are generally consistent, while the residuals of the fixed solution are slightly smaller than those of the float solution, indicating that ambiguity fixing contributes to more precise separation of the receiver clock parameters.

Figure 8 shows the Allan deviation curves of GNSS time-frequency comparison for the links between the CSS and ground stations. The long-term frequency stability for the float solution approaches the 10^{-17} level, while that of the fixed ambiguity solution reaches the 5×10^{-17}. Both solutions deliver comparable stability for short averaging times. For averaging times beyond 200 s, the fixed-ambiguity solution takes a clear lead. This performance disparity widens with longer averaging times, featuring an average enhancement of 10.1% and a peak value of 25.5% at 40,000 s. It is noteworthy that although the short-term and long-term frequency stability of the CSS and ground station clocks can reach the 10^{-16} and 10^{-18} level, respectively, constrained by the accuracy of GNSS carrier phase observations and the dynamic solution mode of the CSS, the short-term and long-term stability of space-ground time-frequency comparison only attains the 10^{-13} and 10^{-17} level.

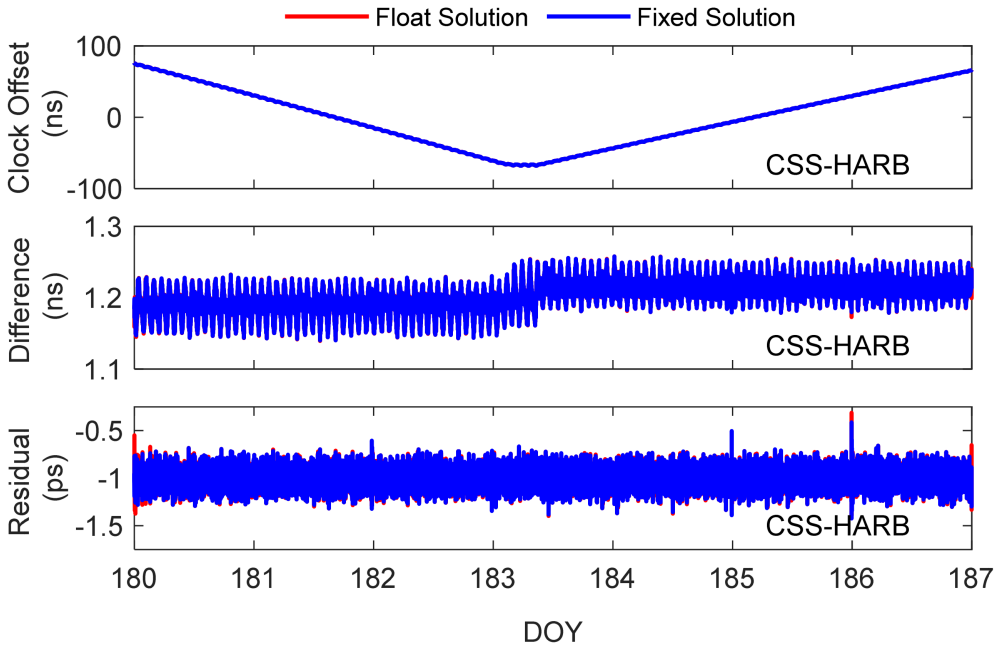


Figure 7. GNSS undifferenced time-frequency comparison results for the CSS-HARB link.

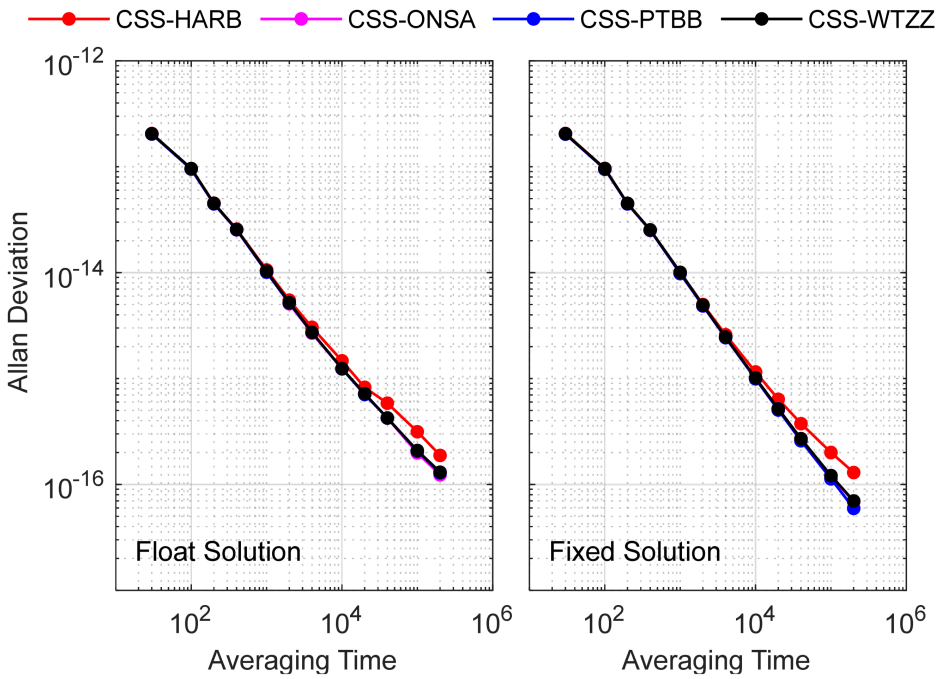


Figure 8. Allan deviation of GNSS undifferenced time-frequency comparison for links between the CSS and ground stations.

To mitigate the noise in GNSS undifferenced time-frequency comparison, the results are converted into frequency offset sequences, and the Vondrak filter is adopted to suppress the high-frequency noise of raw frequency offsets. The filter coefficients are determined via K-fold cross-validation. Figure 9 presents the frequency offset series of the CSS-HARB link before and after Vondrak filtering under both float and fixed ambiguity solutions. The raw frequency offset is contaminated by GNSS observation noise and exhibits prominent fluctuations, which degrade the estimation precision of the gravitational potential. After Vondrak filtering, the filtered frequency offset sequence becomes much smoother.

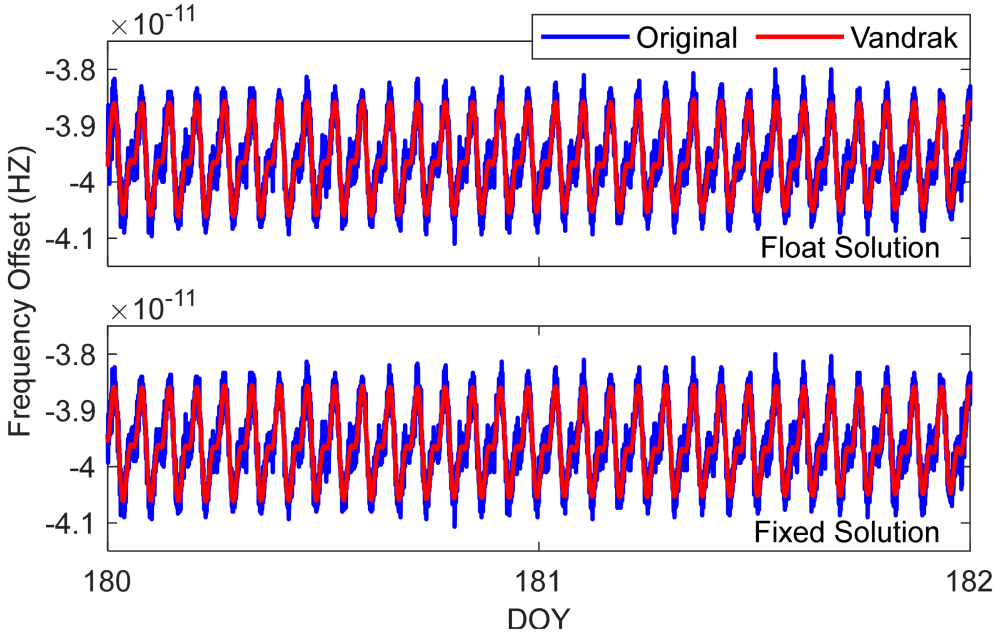


Figure 9. Frequency offset series of the CSS-HARB link.

Table 3 summarizes the Root Mean Square (RMS) of frequency offset residuals before and after Vondrak filtering. It can be observed that the residuals are significantly reduced after filtering for both float and fixed ambiguity solutions. For each link, the relative reduction of residuals ranges from 91.93% to 92.09% under float solutions, and from 92.04% to 92.19% under fixed ambiguity solutions. Compared with the raw frequency offset, the Vondrk filter greatly mitigates the systematic bias associated with geopotential. Ambiguity fixing can further improve the estimation accuracy, with the statistical gain maintained at approximately 92% across all links.

Table 3. RMS of frequency offset residuals before and after Vondrak filtering ($\times 10^{-13}$).

Link	Float Solution		Fixed Solution	
	Original	**Vandrak**	**Original**	**Vandrak**
CSS-HARB	1.848	0.148	1.844	0.145
CSS-ONSA	1.826	0.146	1.826	0.145
CSS-PTBB	1.820	0.144	1.818	0.142
CSS-WTZZ	1.835	0.148	1.834	0.146

5.3. Gravitational Redshift Test via GNSS Time-Frequency Comparison

Taking the gravitational potential difference derived from the EGM2008 gravity field model as the reference, Figure 10 shows the results of the gravitational redshift test based on GNSS undifferenced time-frequency comparison after Vondrak filtering.

From the results in Figure 10, it can be seen that the accuracy of the gravitational redshift test improves continuously with increasing observation time, and the test results across all links are relatively close with good consistency. The gravitational redshift coefficient fluctuates significantly at DOY 180, then converges rapidly by DOY 181, and remains essentially stable after DOY 185. After convergence, both the float solution and the fixed ambiguity solution achieve a gravitational redshift test accuracy on the order of 10^{-7}. Comparing the fixed and float solutions shows that the fixed solution gives higher accuracy in the gravitational redshift test, largely due to its better time-frequency comparison performance.

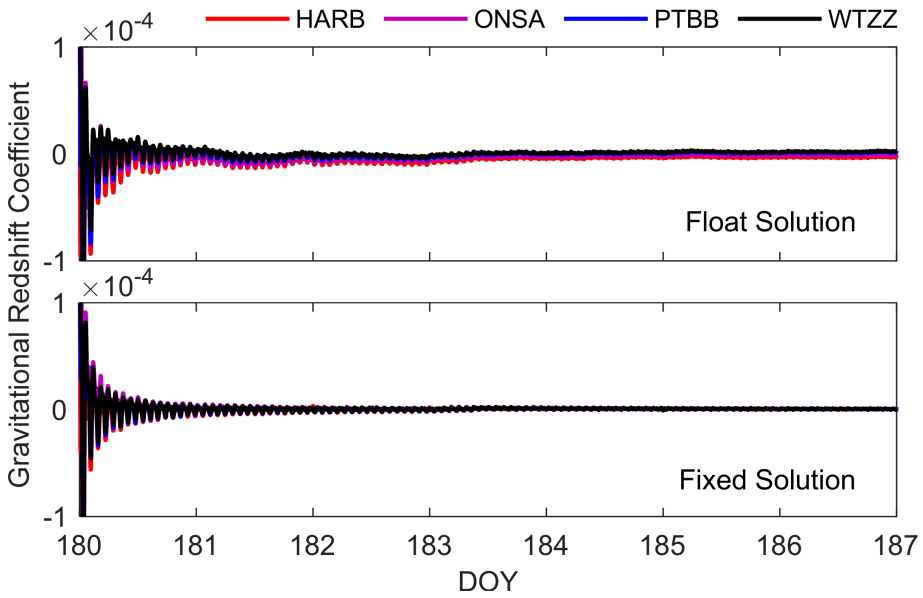


Figure 10. Time series of the gravitational redshift coefficient.

Figure 11 presents the distribution of the gravitational redshift coefficients during the experiment. The boxes cover the upper and lower quartiles, the red lines denote the medians, and the whiskers represent the extreme value ranges of the gravitational redshift coefficient. It should be noted that the gravitational redshift results on DOY 180 have not converged, and the corresponding coefficients are excessively large for clear visualization. Therefore, only the results from DOY 181 to DOY 186 are displayed in the figure. With the accumulation of observation time, the dispersion of the gravitational redshift coefficients gradually narrows, with the interquartile range and the fluctuation range of extreme values continuously decreasing. The results for DOY 185 and DOY 186 tend to be consistent. By comparing the statistical distributions of the float solution and the fixed solution, it can be found that the interquartile width of the box plots for the fixed solution is generally narrower, and the narrowing effect of dispersion becomes more prominent with increasing observation time. This result indicates that ambiguity fixing can effectively eliminate the uncertainty introduced by carrier phase ambiguity and further improve the accuracy and robustness of the gravitational redshift test. Overall, the medians of the gravitational redshift coefficients under both strategies are stable near zero, without significant systematic bias. After convergence, the coefficients are generally on the order of 10^{-7}, among which the fixed ambiguity solution achieves better accuracy.

Table 4 presents the mean values and standard deviations (STDs) of the gravitational redshift test for each link after convergence. Under the float solution mode, the mean test results of each link exhibit certain differences. Specifically, the CSS-HARB link shows the most significant systematic deviation, while the CSS-ONSA link achieves the best overall accuracy. The STD of all links remains stable at approximately 4.0×10^{-7}, indicating comparable random noise levels across different links. After ambiguity fixing, both the mean values and STDs of the gravitational redshift test decrease to varying degrees for each link. The relative reduction of the mean values ranges from about 20% to 84%, and the relative reduction of the STDs is maintained at around 22%. The average result of the gravitational redshift test under the float and fixed ambiguity solutions is $-1.439 \times 10^{-6} \pm 3.972 \times 10^{-7}$ and $6.105 \times 10^{-7} \pm 3.069 \times 10^{-7}$. Previous microwave and laser-link gravitational redshift experiments, which cannot maintain continuous tracking of the CSS, typically require continuous observations spanning several months [31,32,35]. In contrast,

our GNSS undifferenced time-frequency comparison scheme achieves the measurement within only one week under the adopted simulation settings.

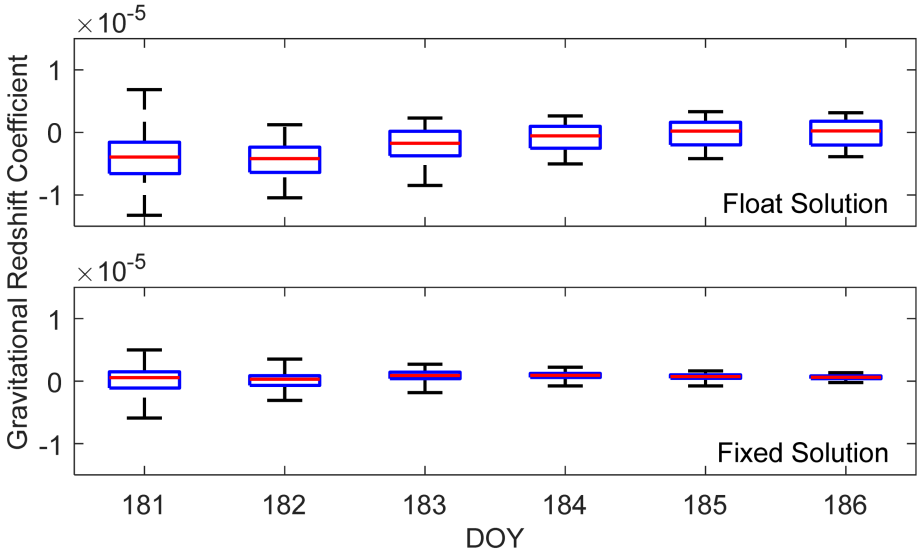


Figure 11. Statistical distribution of the gravitational redshift test coefficient.

Table 4. Mean values and STD of the gravitational redshift test coefficients ($\times 10^{-7}$).

Link	Float Solution		Fixed Solution	
	Mean	**STD**	**Mean**	**STD**
CSS-HARB	−30.416	3.946	4.943	3.135
CSS-ONSA	−9.699	4.050	7.672	3.034
CSS-PTBB	13.854	3.854	5.467	2.975
CSS-WTZZ	20.505	4.039	6.337	3.130

5.4. Determination of Geopotential via GNSS Time-Frequency Comparison

The geopotential difference between the CSS and ground stations is time-varying, which hinders the accuracy statistics. Therefore, this study takes the geopotential of CSS as a known condition and uses the geopotential difference obtained from GNSS time-frequency comparison to invert the geopotential at ground stations. The geopotential of each station is shown in Figure 12.

Figure 12 presents the time series of the geopotential derived from GNSS time-frequency comparison for each ground station. Consistent with the variation pattern of the gravitational redshift test results shown in Figure 9, the amplitude of the geopotential shows a gradually decreasing convergence trend with the increase in observation duration. All links exhibit large oscillations at the initial solution stage of DOY 180, with the peak amplitude exceeding 100 m^2/s^2. As the solution parameters gradually converge, the geopotential amplitude decays rapidly, and the geopotential sequence gradually enters a stable stage after DOY 185. In the float solution, there are obvious differences in the steady-state geopotentials of each link after convergence. Among them, the steady-state geopotential amplitude of the CSS-HARB link is significantly higher than that of the other links, which corresponds to the systematic deviation characteristics of the gravitational redshift test for this link. In contrast, the geopotential sequences of the fixed solution converge faster with smaller steady-state geopotential amplitudes, and the geopotential of all links tends to be consistent.

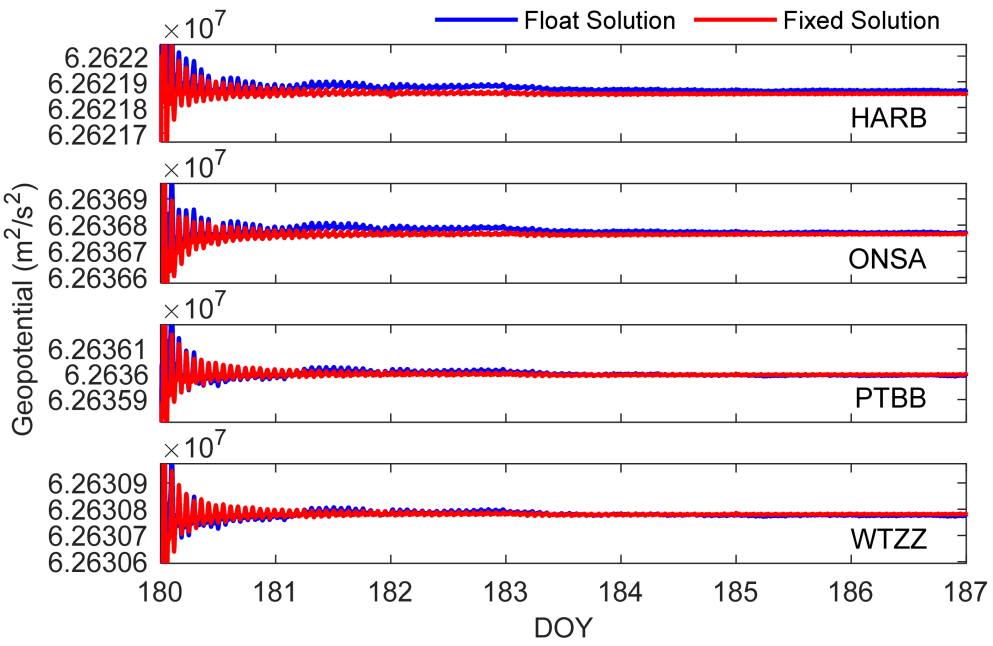


Figure 12. Time series of ground station geopotential determined by GNSS undifferenced time-frequency comparison.

Figure 13 presents the daily boxplot statistical distribution of geopotential deviations between the geopotential derived from GNSS time-frequency comparison for each link and the reference geopotential from the EGM2008 gravity field model during DOY 181–186. In the float solution mode, the overall dispersion of geopotential deviations is relatively high, with the extreme value range close to ± 100 m^2/s^2 at the initial stage (DOY 181). With the accumulation of observation duration, the box width and extreme value range gradually narrow, and the accuracy of the determined geopotential improves gradually. In contrast, the error magnitude of the fixed solution is significantly reduced, with the overall distribution range compressed to within ± 30 m^2/s^2, and the convergence speed is obviously accelerated. After entering DOY 185–186, the interquartile range narrows substantially, and the median deviation stabilizes near the zero value. This indicates that ambiguity fixing effectively eliminates the independent systematic deviation components of each link, which not only improves the determination accuracy of geopotential, but also enhances the consistency of results among different links. This rule is consistent with the previous accuracy analysis results of the gravitational redshift test, and the two conclusions mutually corroborate each other.

Table 5 lists the statistical results of absolute mean and RMS values of geopotential deviations for each link after convergence. In the float solution mode, the RMS of geopotential deviations varies widely across links with remarkable performance discrepancies. The average RMS over all links is 7.043 m^2/s^2, equivalent to a height accuracy of approximately 0.8 m. Noticeable systematic deviations can be identified from the mean values. For instance, the RMS of the CSS-HARB link reaches up to 11.183 m^2/s^2, which indicates that unresolved floating phase ambiguities introduce substantial systematic offsets and thereby shift the solved geopotential results away from the reference values. In contrast, the fixed solution yields a prominent improvement in the accuracy of geopotential estimation, accompanied by a more uniform geopotential deviation distribution and significantly enhanced consistency among different links. The average RMS of all links for fixed solutions is 2.541 m^2/s^2. Taking $g = 9.8$ m/s^2, this value corresponds to an equivalent height of approximately 0.26 m (~0.3 m). Compared with the float solution, the accuracy is improved by approximately 64%. This result demonstrates the advantages of ambiguity-fixed solutions in geopotential

determination via time comparison and further verifies the feasibility and reliability of space-ground GNSS time transfer signals for geopotential determination.

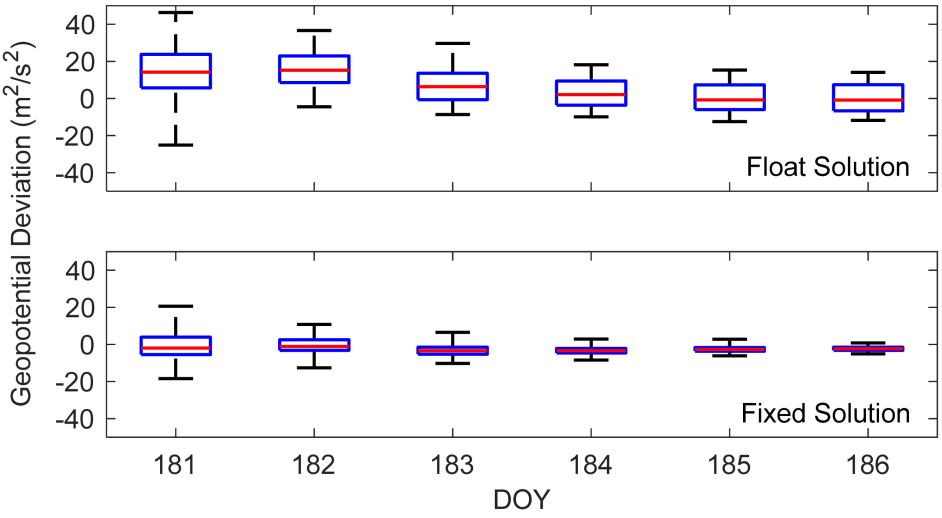


Figure 13. Daily boxplot statistical distribution of geopotential difference deviations.

Table 5. Absolute mean and RMS values of ground station geopotential deviations (m^2/s^2).

Link	Float Solution		Fixed Solution	
	Mean	**RMS**	**Mean**	**RMS**
CSS-HARB	11.182	11.182	1.796	2.134
CSS-ONSA	3.898	3.898	2.862	3.082
CSS-PTBB	5.348	5.348	2.036	2.321
CSS-WTZZ	7.745	7.745	2.352	2.626

6. Discussion

This work conducts joint gravitational redshift tests and geopotential measurement using simulated GNSS undifferenced carrier phase observations constrained by the CSS. The determined geopotential achieves decimeter-level equivalent height accuracy, and the gravitational redshift result reaches the 10^{-7} magnitude. While this gravitational redshift result is comparable to that of previous optical and microwave link experiments, conventional ground-based microwave or optical schemes rely on dedicated space-ground links and usually require continuous observations spanning several months. In contrast, this study utilizes existing GNSS undifferenced carrier phase signals without constructing additional dedicated hardware for time-frequency comparison, offering global coverage and low cost.

Nevertheless, limited by the noise of GNSS observables and the dynamic solution model of the CSS, the performance of space-ground time-frequency comparison and the accuracy of geopotential determination are restricted to some extent. Hence, high-precision space-ground GNSS time-frequency comparison schemes remain to be further explored.

It should be noted that this study is a simulation study, and all observed values and clock offset data are generated synthetically. Future work will explore the use of real in-orbit GNSS measurement data from the CSS, expand the ground-station network, exploit multi-frequency observations and PPP-AR, and refine error correction models, with the aim of gradually improving the capability of gravitational redshift testing and geopotential determination.

7. Conclusions

This study investigates the impact of anticipated optical clock hardware onboard the Mengtian laboratory module of the CSS on gravitational redshift testing and geopotential determination using GNSS undifferenced carrier phase time-frequency signals. Based on the simulation of GNSS observations and optical clock offsets, one week of GNSS observations from four ground stations are selected to perform simulation experiments of gravitational redshift testing and geopotential determination. The simulation results show that the gravitational redshift test results derived from GNSS time-frequency comparison reach 6.1×10^{-7} with a STD of 3.1×10^{-7}, representing an improvement of one order of magnitude over the highest accuracy of existing GNSS-based measured gravitational redshift results. Taking the EGM2008 gravity field model values as reference, the RMS of the geopotential deviation at ground stations determined via GNSS time-frequency comparison reaches 2.5 m^2/s^2, corresponding to an equivalent height error of approximately 0.3 m. Compared with the conventional intermittent comparison approach where ground stations observe space station signals, the GNSS time-frequency comparison technique enables continuous time synchronization between the CSS and ground stations and demonstrates prominent technical advantages. With continuous improvements in atomic clock performance and gradual reduction in costs, optical clocks will be widely deployed on various satellite platforms in the future. Combined with improved GNSS satellite Products, GNSS time-frequency comparison models and refined GNSS error models, centimeter-level equivalent-height geopotential determination will gradually become achievable using high-precision space-borne optical clocks. Such capability would facilitate the unification of the global height datum.

Author Contributions: Conceptualization, W.X.; methodology, W.X. and J.S.; software, W.X.; validation, W.X. and P.Z.; formal analysis, W.X.; investigation, W.X.; resources, W.X.; data curation, X.L.; writing—original draft preparation, W.X. and X.L.; writing—review and editing, W.X., X.L. and J.S.; Visualization, W.X., P.Z. and J.S. All authors have read and agreed to the published version of the manuscript.

Funding: This research was funded by the National Natural Science Foundation of China (No. 42304095), the Key Project for Training of Outstanding Young Teachers in Anhui Province (No. YQZD2026063), the Key Project of Natural Science Research in Universities of Anhui Province (No. 2023AH051634) and the Chuzhou University Research Initiation Fund Project (No. 2023qd07, No. 2026qd02).

Data Availability Statement: The GNSS satellite products are available at ftp://igs.gnsswhu.cn/pub (accessed on 15 November 2026). The simulation dataset can be provided upon reasonable request.

Acknowledgments: We thank the IGS for providing GNSS satellite products in this research.

Conflicts of Interest: The authors declare no conflicts of interest.

References

1. Mehlstäubler, T.E.; Grosche, G.; Lisdat, C.; Schmidt, P.O.; Denker, H. Atomic clocks for geodesy. *Rep. Prog. Phys.* **2018**, *81*, 064401. [CrossRef] [PubMed]
2. Zheng, X.; Dolde, J.; Lochab, V.; Merriman, B.N.; Li, H.; Kolkowitz, S. Differential clock comparisons with a multiplexed optical lattice clock. *Nature* **2022**, *602*, 425–430. [CrossRef] [PubMed]
3. Pound, R.V.; Rebka, G.A., Jr. Gravitational red-shift in nuclear resonance. *Phys. Rev. Lett.* **1959**, *3*, 439. [CrossRef]
4. Pound, R.V.; Snider, J.L. Effect of gravity on gamma radiation. *Phys. Rev.* **1965**, *140*, B788. [CrossRef]
5. Vessot, R.F.C.; Levine, M.W. A test of the equivalence principle using a space-borne clock. *Gen. Relativ. Gravit.* **1979**, *10*, 181–204. [CrossRef]
6. Vessot, R.F.; Levine, M.W.; Mattison, E.M.; Blomberg, E.L.; Hoffman, T.E.; Nystrom, G.U.; Farrel, B.F.; Decher, R.; Eby, P.B.; Baugher, C.R.; et al. Test of relativistic gravitation with a space-borne hydrogen maser. *Phys. Rev. Lett.* **1980**, *45*, 2081. [CrossRef]
7. Vessot, R.F. Clocks and spaceborne tests of relativistic gravitation. *Adv. Space Res.* **1989**, *9*, 21–28. [CrossRef]

8. Chou, C.W.; Hume, D.B.; Rosenband, T.; Wineland, D.J. Optical clocks and relativity. *Science* **2010**, *329*, 1630–1633. [CrossRef] [PubMed]
9. Grotti, J.; Koller, S.; Vogt, S.; Häfner, S.; Sterr, U.; Lisdat, C.; Heinecke, D.; Riedmann, S.; Dehms, T.; Huntemann, N.; et al. Geodesy and metrology with a transportable optical clock. *Nat. Phys.* **2018**, *14*, 437–441. [CrossRef]
10. Takamoto, M.; Ushijima, I.; Ohmae, N.; Yahagi, T.; Kokado, K.; Shinkai, H.; Katori, H. Test of general relativity by a pair of transportable optical lattice clocks. *Nat. Photon.* **2020**, *14*, 411–415. [CrossRef]
11. Li, Y.; Liu, T.; Pei, Y.; Guan, H.; Leng, J.; Shuai, T.; Wang, H.; Gao, Y. Gravitational redshift test in a lunar distant retrograde orbit using a compact hydrogen maser. *Chin. Phys. Lett.* **2026**, *43*, 031101. [CrossRef]
12. Kentosh, J.; Mohageg, M. Global positioning system test of the local position invariance of Planck's constant. *Phys. Rev. Lett.* **2012**, *108*, 110801. [CrossRef] [PubMed]
13. Delva, P.; Hees, A.; Bertone, S.; Richard, E.; Wolf, P. Test of the gravitational redshift with stable clocks in eccentric orbits: Application to Galileo satellites 5 and 6. *Class. Quantum Grav.* **2015**, *32*, 232003. [CrossRef]
14. Herrmann, S.; Finke, F.; Lülf, M.; Kichakova, O.; Puetzfeld, D.; Knickmann, D.; List, M.; Rievers, B.; Giorgi, G.; Günther, H.; et al. Test of the gravitational redshift with Galileo satellites in an eccentric orbit. *Phys. Rev. Lett.* **2018**, *121*, 231102. [CrossRef] [PubMed]
15. Delva, P.; Puchades, N.; Schönemann, E.; Dilssner, F.; Courde, C.; Bertone, S.; Gonzalez, F.; Hees, A.; Le Poncin-Lafitte, C.; Meynadier, F.; et al. A new test of gravitational redshift using Galileo satellites: The GREAT experiment. *C. R. Phys.* **2019**, *20*, 176–182. [CrossRef]
16. Litvinov, D.; Pilipenko, S. Testing the Einstein equivalence principle with two Earth-orbiting clocks. *Class. Quantum Grav.* **2021**, *38*, 135010. [CrossRef]
17. Delva, P.; Puchades, N.; Schönemann, E.; Dilssner, F.; Courde, C.; Bertone, S.; Gonzalez, F.; Hees, A.; Le Poncin-Lafitte, C.; Meynadier, F.; et al. Gravitational redshift test using eccentric Galileo satellites. *Phys. Rev. Lett.* **2018**, *121*, 231101. [CrossRef] [PubMed]
18. Takano, T.; Takamoto, M.; Ushijima, I.; Ohmae, N.; Akatsuka, T.; Yamaguchi, A.; Katori, H. Geopotential measurements with synchronously linked optical lattice clocks. *Nat. Photon.* **2016**, *10*, 662–666. [CrossRef]
19. Lisdat, C.; Grosche, G.; Quintin, N.; Shi, C.; Raupach, S.M.F.; Grebing, C.; Nikitin, B.; Altin, M.; Amairi, S.; Bange, S.; et al. A clock network for geodesy and fundamental science. *Nat. Commun.* **2016**, *7*, 12443. [CrossRef] [PubMed]
20. Shen, Z.; Shen, W.; Peng, Z.; Liu, T.; Zhang, S.; Chao, D. Formulation of determining the gravity potential difference using ultra-high precise clocks via optical fiber frequency transfer technique. *J. Earth Sci.* **2019**, *30*, 422–428. [CrossRef]
21. Huang, Y.; Zhang, H.; Zhang, B.; Hao, Y.; Guan, H.; Zeng, M.; Gao, K. Geopotential measurement with a robust, transportable Ca+ optical clock. *Phys. Rev. A* **2020**, *102*, 050802. [CrossRef]
22. Liu, D.; Wu, L.; Xiong, C.; Bao, L. Geopotential difference measurement using two transportable optical clocks' frequency comparisons. *Remote Sens.* **2024**, *16*, 2462. [CrossRef]
23. Yuan, Y.; Cui, K.; Liu, D.; Yuan, J.; Cao, J.; Wang, D.; Zhang, X. Demonstration of chronometric leveling using transportable optical clocks beyond laser coherence limit. *Phys. Rev. Appl.* **2024**, *21*, 044052. [CrossRef]
24. Lee, J.; Kwon, J.H.; Park, C.Y.; Kim, H.; Choi, I.M.; Chung, J.W.; Lee, W.K. Evaluation of the relativistic redshift in frequency standards at KRISS. *Metrologia* **2024**, *61*, 015008. [CrossRef]
25. Xu, W.; Zhang, P. Determining of geopotential difference with multi-GNSS undifferenced time-frequency signals. *IEEE Trans. Instrum. Meas.* **2026**, *75*, 6505010. [CrossRef]
26. Wang, L.; Shen, W.; Fok, H.S.; Li, L.; Zhang, P.; Shen, Z.; Xu, W.; Wu, K. Experiment of geopotential measurement using GNSS single-clock transportation method. *Geophys. J. Int.* **2025**, *242*, ggaf223. [CrossRef]
27. Wu, K.; Shen, W.B.; Fok, H.S.; Lian, Z.; Zhang, P.; Li, L.; Wang, L.; Shen, Z. Measuring intercontinental-scale geopotential difference using atomic clock frequency comparison with PPP technique. *Adv. Space Res.* **2025**, *77*, 472–490. [CrossRef]
28. Xu, W.; Yan, C.; Zhang, P. GNSS carrier phase time and frequency comparison for gravity potential determination. *Geophys. J. Int.* **2026**, *244*, ggaf479. [CrossRef]
29. Wu, K.; Shen, W.B.; Shen, Z.; Fok, H.S.; Guo, Y.; Li, K.; Wang, L.; Guo, H. Precise cross-sea orthometric height determination using GNSS carrier-phase time-frequency transfer. *Remote Sens.* **2025**, *17*, 3949. [CrossRef]
30. Savalle, E.; Guerlin, C.; Delva, P.; Meynadier, F.; Le Poncin-Lafitte, C.; Wolf, P. Gravitational redshift test with the future ACES mission. *Class. Quantum Grav.* **2019**, *36*, 245004. [CrossRef]
31. Sun, X.; Shen, W.B.; Shen, Z.; Cai, C.; Xu, W.; Zhang, P. Test of gravitational red-shift based on tri-frequency combination of microwave frequency links. *Eur. Phys. J. C* **2021**, *81*, 634. [CrossRef]
32. Shen, W.; Zhang, P.; Shen, Z.; Xu, R.; Sun, X.; Ashry, M.; Wang, C.; Cai, C. Testing gravitational redshift based on microwave frequency links onboard the China Space Station. *Phys. Rev. D* **2023**, *108*, 064031. [CrossRef]
33. Zhang, P.; Shen, W.B.; Wang, C.; Shen, Z.; Cai, C.; Sun, X.; Ashry, M. Higher order ionospheric effects in testing gravitational redshift by space frequency signal transfer. *Astron. Astrophys.* **2023**, *679*, A86. [CrossRef]

34. Qin, C.G.; Liu, T.; Dai, X.Y.; Guo, P.B.; Huang, W.; Liu, X.P.; Zhang, H.; Shao, C.G. Preliminary sensitivity study for a gravitational redshift measurement with China's Lunar exploration project. *Class. Quantum Grav.* **2024**, *41*, 135006. [CrossRef]
35. Xu, R.; Shen, W.; Fok, H.S.; Zhang, P.; Li, L.; Wang, L.; Shen, Z.; Pan, Y. Formulation of testing gravitational redshift based on laser time link between China Space Station and a ground station. *Eur. Phys. J. C* **2026**, *86*, 818. [CrossRef]
36. Dai, X.Y.; Qin, C.G.; Gong, Q.L.; Ma, Z.Y.; Tan, Y.J.; Shao, C.G. Sensitivity analysis of gravitational redshift tests using atomic-clock phase measurements onboard the China Space Station. *Phys. Rev. D* **2026**, *114*, 064073. [CrossRef]
37. Enzer, D.; Yu, N. Frequency-analysis approach for ACES space-clock comparisons to extract gravitational redshift. *Class. Quantum Grav.* **2026**, *43*, 015013. [CrossRef]
38. Zhang, P.F.; Wang, C.X.; Li, L.H.; Wang, L.; Shen, Z.Y.; Xu, R.; Shen, W.B. Gravity potential determination based on China Space Station dual-frequency microwave links frequency transfer. *arXiv* **2024**, arXiv:2501.00304.
39. Zhang, P.; Wang, C.; Xu, W. Research on the modified tri-frequency combination model for determining geopotential using China space station microwave links. *iScience* **2026**, *29*, 115869. [CrossRef] [PubMed]
40. Lachmann, K.E.; Müller, J.; Vollmair, P.; Schlicht, A. Determination of physical height differences from time transfer via the ACES mission—A simulation study. *arXiv* **2026**, arXiv:2609.21786.
41. Leick, A.; Rapoport, L.; Tatarnikov, D. *GPS Satellite Surveying*, 4th ed.; Wiley: Hoboken, NJ, USA, 2015.
42. Xu, W.; Shen, W.; Cai, C. Comparison and evaluation of carrier phase PPP and single difference time transfer with multi-GNSS ambiguity resolution. *GPS Solut.* **2023**, *26*, 58. [CrossRef]
43. Sun, H.; Shen, W.; Gao, K.; Gao, Y.; Hou, M.; Bao, L.; Shen, Z. Advances in time-frequency based geopotential determination. *Geod. Geodyn.* **2026**, *17*, 12–24. [CrossRef]
44. Panfilo, G.; Tavella, P. Atomic clock prediction based on stochastic differential equations. *Metrologia* **2008**, *45*, S108–S116. [CrossRef]
45. Galleani, L.; Sacerdote, L.; Tavella, P.; Zucca, C. A mathematical model for the atomic clock error. *Metrologia* **2003**, *40*, S257–S264. [CrossRef]
46. Shen, W.; Zhang, P.; Shen, Z.; Xu, R.; Gao, Y. Simulation test of gravitational redshift by microwave links of China space station. *Geomat. Inf. Sci. Wuhan Univ.* **2022**, *47*, 849–854.
47. Petit, G.; Luzum, B. The 2010 reference edition of the IERS conventions. In *Reference Frames for Applications in Geosciences*; Springer: Berlin/Heidelberg, Germany, 2012; pp. 57–61.
48. Lyard, F.; Lefevre, F.; Letellier, T.; Francis, O. Modelling the global ocean tides: Modern insights from FES2004. *Ocean Dyn.* **2006**, *56*, 394–415. [CrossRef]
49. Saastamoinen, J. Contributions to the theory of atmospheric refraction. *Bull. Géod.* **1972**, *105*, 279–298. [CrossRef]
50. Böhm, J.; Heinkelmann, R.; Schuh, H. Short note: A global model of pressure and temperature for geodetic applications. *J. Geod.* **2007**, *81*, 679–683. [CrossRef]
51. Böhm, J.; Niell, A.; Tregoning, P.; Schuh, H. Global mapping function (GMF): A new empirical mapping function based on numerical weather model data. *Geophys. Res. Lett.* **2006**, *33*, L07304. [CrossRef]
52. Byun, S.H.; Bar-Sever, Y.E. A new type of troposphere zenith path delay product of the international GNSS service. *J. Geod.* **2009**, *83*, 1–7. [CrossRef]
53. Wang, Q.; Zhu, J.; Yang, G. Characteristic analysis of the differences between total electron content (TEC) values in global ionosphere map (GIM) grids. In *Annales Geophysicae*; Copernicus Publications: Göttingen, Germany, 2024; Volume 42, pp. 45–53.
54. Geng, J.; Zhang, Q.; Li, G.; Liu, J.; Liu, D. Observable-specific phase biases of Wuhan multi-GNSS experiment analysis center's rapid satellite products. *Satell. Navig.* **2022**, *3*, 23. [CrossRef]
55. Pavlis, N.K.; Holmes, S.A.; Kenyon, S.C.; Factor, J.K. The development and evaluation of the Earth Gravitational Model 2008 (EGM2008). *J. Geophys. Res. Solid Earth* **2012**, *117*, B04406. [CrossRef]
56. Wu, J.T.; Wu, S.C.; Hajj, G.A.; Bertiger, W.I.; Lichten, S.M. Effects of antenna orientation on GPS carrier phase. *Manuscripta Geod.* **1993**, *18*, 91–98. [CrossRef]

Disclaimer/Publisher's Note: The statements, opinions and data contained in all publications are solely those of the individual author(s) and contributor(s) and not of MDPI and/or the editor(s). MDPI and/or the editor(s) disclaim responsibility for any injury to people or property resulting from any ideas, methods, instructions or products referred to in the content.